CARBON 65 (2013) 252–260

Available at www.sciencedirect.com

ScienceDirect

journal homepage: www.elsevier.com/locate/carbon

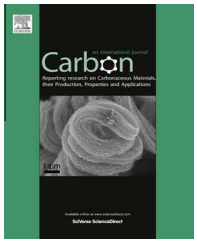

Synthesis and transport properties of $La_{0.67}Sr_{0.33}MnO_3$ conformally-coated on carbon nanotubes

Juan Beltran-Huarac [a,b,*], *Jennifer Carpena-Nuñez* [b], *Danilo Barrionuevo* [b], *Frank Mendoza* [a,b], *Ram S. Katiyar* [a,b], *Luis F. Fonseca* [a,b], *Brad R. Weiner* [a,c], *Gerardo Morell* [a,b]

[a] *Institute for Functional Nanomaterials, University of Puerto Rico, San Juan, PR 00931, USA*
[b] *Department of Physics, University of Puerto Rico, San Juan, PR 00936, USA*
[c] *Department of Chemistry, University of Puerto Rico, San Juan, PR 00936, USA*

ARTICLE INFO

Article history:
Received 1 June 2013
Accepted 16 August 2013
Available online 23 August 2013

ABSTRACT

We report for the first time the fabrication of nanostructured ferromagnetic lanthanum strontium manganite $La_{0.67}Sr_{0.33}MnO_3$ (LSMO) conformally coated onto bamboo-like carbon nanotubes (BCNTs) by pulsed laser deposition. Scanning electron microscopy revealed that one-dimensional LSMO/BCNTs with diameters ranging from 100-160 nm and lengths over 10 μm were obtained. Line-scanned energy-dispersive X-ray spectroscopy profiles, selected area electron diffraction rings, and energy-filtered transmission electron microscopy maps provided further insight into the hybrid nanostructures. LSMO/BCNT and BCNT were also investigated via *in situ* electrical probing in a transmission electron microscope using a piezo-driven scanning tunneling microscopy holder. Modeling of the *I*–*V* characteristics of individual hybrid nanotubes yielded the resistivity, bandgap, and electron density of LSMO and BCNT. The results show that the transport properties of LSMO/BCNT are superior to those of BCNT. This research advances the integration of oxide materials and carbon nanotubes, bringing forth new avenues for miniaturization and fabrication of one-dimensional core-multishell materials with multifunctional properties that can be used as building blocks in nanodevices.

1. Introduction

For decades, many efforts in electronics have been focused on new miniaturization strategies. The use of a single-organic molecule for electronic devices, such as a simple molecular rectifier was first proposed in 1974 by Aviram and Ratner [1]. Since then, this powerful idea has been conceptually sharpened and experimentally tested in the expectation that it would open up new ways for achieving good electrical contacts between bulk electrodes and individual molecules, a long-standing problem that still remains unsolved in nanoelectronics.

A single-walled carbon nanotube (SWCNT) based field-effect transistor was one of the first systems studied and it has provided the most promising results. For instance, the electrical resistance in these transistors is controllable by adjusting the gate voltage and the conduction in nanotubes is considered ballistic. Therefore, SWCNTs open up the

* *Corresponding author.*
E-mail address: baristary26@gmail.com (J. Beltran-Huarac).
0008-6223/$ - see front matter
http://dx.doi.org/10.1016/j.carbon.2013.08.023

possibility of manufacturing less power-consuming and faster devices [2–4], breaking barriers beyond the silicon roadmap. SWCNTs are however difficult to isolate, which hampers their applications.

Multi-walled carbon nanotubes (MWCNTs), on the other hand, are easier to manipulate and friendlier for the design of devices. Several studies have recently reported that bamboo-like carbon nanotubes (BCNTs) present a higher edge-to-plane ratio and abundant dangling bonds on the outer surface and in the inner channel than conventional seamless MWCNTs, rendering them more suitable for a wider range of applications in nanoelectronics [5,6]. The periodic structure of BCNTs encompasses walls of sp^2-bonded carbon and lateral borders that are sp^3-bonded [7–9]. To date, BCNTs have been overlooked as a channel material in field-effect transistors and as an enabler for the integration of ferromagnetic oxides into nanodevices.

It has been established that an electrical current can flow through a SWCNT having two half-metallic oxides as electrodes [10,11]. The contact resistance of this system is only double the value obtained for a SWCNT/standard electrode at room temperature (RT) [10]. This increased interfacial resistance is similar to that found for contacts between manganites and metals [12]. In particular, interfaces between lanthanum strontium manganite $La_{0.67}Sr_{0.33}MnO_3$ (LSMO) and metals have shown to be similar to a tunnel barrier [12].

It is well-known that LSMO exhibits high spin polarization, half-metallic-like transport, ferromagnetism at RT (T_c = 360 K), a colossal magnetoresistance effect, and electronic behavior conducive to nanospintronics and nanoelectronics [13–15]. To date, there are no reports on the fabrication of LSMO nanotubes or their integration with CNTs. Exploratory research has been reported on the synthesis of micro-sized-thick tubes via the pore wetting technique [13] and amorphous LSMO nanowires have been grown by electrospinning [14] and template-assisted chemical [15] routes. Some reports claim to have synthesized isolated nanocrystals of LSMO chemically bound to CNTs, but this is far from being a conformal coating [16,17].

The transport properties of individual LSMO conformally coated onto CNTs would likely outperform those of CNTs alone and would enable the facile integration of oxide materials onto CNTs, which would represent a key step in nanoelectronics. However, no accounts on the fabrication of one-dimensional LSMO/CNTs have been reported yet, owing principally to the notion that the growth conditions for mixed-valent manganese oxides would destroy CNTs. One likely fabrication method for these hybrids would be pulsed laser deposition (PLD), however, the conditions to grow LSMO under the harsh conditions involving high temperatures, significant oxygen partial pressures, and aggressive frontal collision of massive oxides, have hindered this application to date.

We report here for the first time the fabrication of nanostructured LSMO conformally coated onto BCNTs by PLD. This study establishes the experimental conditions necessary to deposit LSMO on BCNT, thus solving the above-mentioned challenge, and determines the transport properties of the individual LSMO/BCNT hybrid material.

2. Experimental

2.1. Synthesis of LSMO/BCNTs

BCNT films were grown on 1.4 cm-diameter polished copper disks (GoodFellow, 99.9%). Clean Cu substrates were completely covered by catalytic NiO nanoparticles (Alfa Aesar, 99%) and placed in a custom-built HF-CVD chamber [18]. A gas mixture of CH_4 (2%) diluted in H_2 as carbon precursor gas combined with a trace of H_2S (500 ppm, H_2S:H_2) at 100 sccm was introduced into the chamber. The Re filament (2500 °C) was kept at a distance of 8 mm from the substrate. The substrate temperature was fixed at 700 °C while the chamber pressure was kept at 2.7 kPa for 10 min.

The PLD target made of LSMO was prepared by a solid-state reaction route as reported elsewhere [19] using high purity (99.9%) La_2O_3, SrO and MnO_2 (La:Sr:Mn = 0.67:0.33:1.0) as starting raw chemicals. Precursors were stoichiometrically mixed in methanol and high-energy ball-milled for 10 h. The soft mixture was next dried and ground to break up some agglomerates. The resultant powder was first calcined at 400 °C for 3 h to remove organic by-products and then at 1200 °C for 8 h. The calcined products were ball-milled again for 1 h and crushed to fine powder. Polyvinyl alcohol (PVA) was added to the powder, which was then uniaxially pressed (isostatic pressure = 8 tons) into a 25 mm-diameter and 5 mm-thick target. The target was sintered first at 400 °C for 3 h, and then at 1300 °C for 4 h in a covered crucible with alumina powder.

The deposition of LSMO onto BCNT and Cu using the as-prepared target was carried out in a PLD chamber with a KrF excimer laser (Lambda Physik COMPex 205i, 248 nm). The base pressure was 1.3×10^{-4} Pa before starting the ablation process. The substrate-target frontal distance was kept at 4.5 cm. Up to ~70 nm of LSMO was deposited by using ~1000 pulses, 5 Hz and laser energy of 200–280 mJ. The growth temperature and oxygen pressure were 600 °C and 1.1 kPa, respectively. Finally, the LSMO was annealed *in situ* at 500–700 °C at 42.7 kPa.

2.2. Characterization

The structural analysis of the hybrid was studied by means of an X-ray Diffractometer (XRD), Model Siemens D5000 using Cu K_α radiation. Raman spectra were collected using a Jobin–Yvon T64000 spectrometer with Ar-ion laser excitation (514.5 nm). The surface morphology, elemental composition and topography were analyzed using a JEOL JSM-7500F field-emission scanning electron microscope (FE-SEM), a Carl Zeiss Leo 922 transmission electron microscope (TEM), and a JEOL JEM-2200FS high-Cs probe-corrected high-resolution transmission electron microscope (HR-TEM).

For *in situ* experiments, electrical characterization was performed with a piezo-driven STM holder (Nanofactory Instruments AB, STM-TEM) within the TEM chamber. BCNTs and LSMO/BCNTs were detached from the Cu substrate using a diamond tip, then suspended in ethanol and carefully ultrasonicated. The suspension was deposited on a glass surface and once the solvent was completely evaporated, the BCNTs

and LSMO/BCNTs were physically contacted with a 250 μm-thick Au wire. The so-arranged sample was dried overnight to eliminate any remaining trace of the solvent. The counter electrode (Au STM tip) was fabricated from a 250 μm-thick Au wire via electrochemical etching [20]. An electrolyte solution containing 20% $CaCl_2$, Pt electrodes and an arbitrary waveform generator (Agilent, 33220A 20 MHz Function/Arbitrary Waveform Generator) were employed to electrochemically etch the Au tips. An AC potential of 2.45 V with a 1 kHz oscillating frequency and a DC offset of +2.55 V were used to ensure reduction of the Au. This procedure produced tips with a diameter down to 100 nm. The Au tip was then cleaned with ethanol. The sample and tip were next mounted in the STM-TEM specimen holder. Rough alignment of the sample and STM tip was performed in air prior to insertion into the TEM chamber using an optical microscope. The tip was brought in contact with the selected BCNT and LSMO/BCNT by Z-height and sample position adjustment via a piezo-driven stage. In our electrical transport studies, conditioning testing was first executed by applying a high bias until the current readout was stable. LSMO/BCNT showed an improved electrical signal under ±1 V with a smoother hysteresis, lower noise level and smaller deviation. Several BCNTs and LSMO/BCNTs were individually tested over fifteen times each at different longitudinal positions in order to obtain the aggregated *I–V* curves that represent the characteristic electrical behavior of both types of nanotubes. Only semiconducting BCNTs were considered in this investigation.

3. Results and discussion

The XRD patterns of LSMO, BCNTs and LSMO/BCNTs films are shown in Fig. 1a, wherein the diffractogram of copper is included as reference. The diffraction planes (121), (110), (112), (022), (220), (312), (041), (400) found for 70 nm-thick LSMO can be indexed to its orthorhombic (*Pnma*) perovskite structure [14]. No secondary phases were seen indicating the high quality of the sample. Only one diffraction plane (002) was observed for 1 μm-thick BCNTs which is ascribed to the graphitic nature of nanotubes. It was also found that LSMO crystallized rather well in its orthorhombic perovskite structure (see well-defined XRD peaks in Fig. 1a) when deposited onto BCNTs/Cu just as on Cu substrates. LSMO/BCNTs also exhibit a weak signal of graphitic carbon corresponding to BCNTs supporting that both phases co-exist in the hybrid. The lattice parameters of LSMO were $a = 5.397$ Å, $b = 7.345$ Å, $c = 5.601$ Å. The broadening of the LSMO/BCNT diffraction peaks is attributed to the nanocrystalline nature of the sample. The calculated average crystallite size was estimated by means of Scherrer's formula, yielding ~9 nm.

Raman scattering spectra of LSMO, BCNTs and LSMO/BCNTs are shown in Fig. 1b. A broad band centered at 630.9 cm^{-1} characteristic of orthorhombic LSMO was found. This band, denoted by B_{2g} [21], is associated to the stretching and bending of MnO_6 octahedra, and is slightly red-shifted when compared to bulk LSMO, due to the internal tensile-strain between the substrate and the thin film developed during the growth process. Additionally, two low-frequency (298 cm^{-1}, 344.1 cm^{-1}) and one asymmetric second-order (1120 cm^{-1}) Raman-active modes were observed, and correlate to LSMO, with a slight blue-shift as compared to the basic matrix, $LaMnO_3$, owing to the increased Sr content. Two distinctive bands peaking at 1351.1 cm^{-1} and 1583.7 cm^{-1} can be ascribed to the disorder-induced characteristic of graphitic carbon (D band) and to the graphite structure due to the bond stretching of all pairs of sp^2 carbon (G band), respectively [22]. These two high-frequency bands along with an I_G/I_D ratio <1 constitute the fingerprint of BCNTs. There is no radial breathing as expected for BCNTs. Raman-active modes of both LSMO and BCNTs were observed in LSMO/BCNT hybrids demonstrating that orthorhombic perovskite LSMO was successfully crystallized onto BCNTs without any deterioration. Note that a high degree of structural quality was achieved despite the high deposition temperature of LSMO. This fact correlates quite well with the long-range order of LSMO found in the XRD analysis. Additionally, there is both a drop in Raman intensity and decrease in bandwidth of the D and G bands for LSMO/BCNT that is likely attributed to the more pronounced stress existing in the hybrid material [23]. The G and D bands of BCNTs and LSMO/BCNTs were simulated using the damped harmonic oscillator phonon model (DHOPM) [24], showing that the phonon frequency remained almost constant but the bandwidth decreased by ~9 cm^{-1}, as shown in Fig. 1b, providing further evidence that BCNTs endure the LSMO

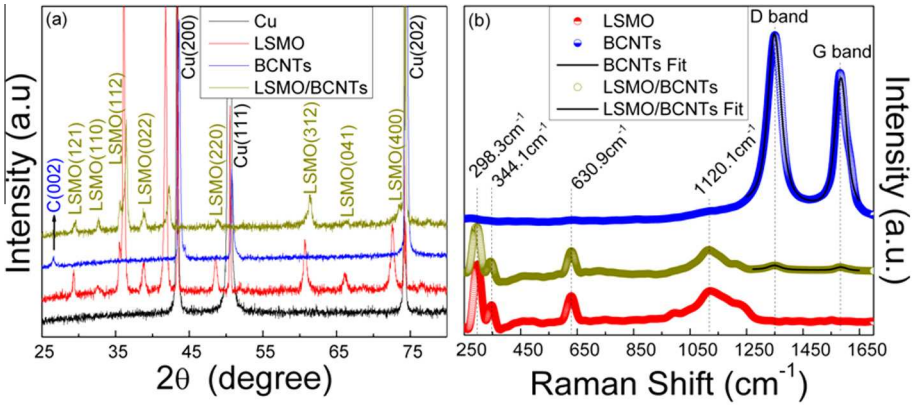

Fig. 1 – XRD patterns (a) and micro-Raman spectra (b) of as-grown LSMO, BCNTs and LSMO/BCNTs films. Solid lines in (b) correspond to the DHOPM fit.

deposition without deteriorating their microstructural quality.

The FE-SEM images of BCNTs before and after LSMO deposition are depicted in Fig. 2 at different magnifications. Smooth BCNTs randomly distributed across the substrate with diameters varying from 80 to 100 nm and lengths >10 μm were observed as shown in Fig. 2a–c. No sign of the catalytic material was found located on the ends of these concentrically rolled sp^2-carbon sheets indicating that they grow with the catalyst at the base (i.e., base-growth model). BCNTs uniformly coated with LSMO are shown in Fig. 2d–f. This conformal coating is the result of the homogeneous LSMO-based plasma that is produced within the PLD reactor [23–26] and the separation among individual BCNTs that is bigger than the nanocrystallites stemming from the PLD target. As a result, the outer BCNTs have a thicker LSMO coating than the inner ones.

The length of BCNTs was retained after LSMO deposition, albeit the outer diameter was raised to 120–180 nm as a result of the LSMO coating deposited. Due to their geometry and outer edges (see Fig. 2f), these LSMO/BCNTs heterostructures are expected to pave inroads for additional surface functionalization.

The TEM micrograph of BCNT along with the HR-TEM micrographs, line-scanned energy-dispersive X-ray spectroscopy (EDS) profile, selected area electron diffraction (SAED) rings and energy-filtered TEM (EF-TEM) image of LSMO/BCNTs are depicted in Fig. 3. The morphology and quality of BCNTs are shown in Fig. 3a, wherein characteristic empty internal regions with nano-cavities surrounded by closed walls consisting of a number of layers are observed. After deposition, the thickness of LSMO in LSMO/BCNT was found to be ~20 nm for inner BCNTs and ~40 nm for outer BCNTs (see Fig. 3b), consistent with the thickness of around 70 nm for LSMO deposited on Cu substrate which was determined by taking SEM cross-sections. The LSMO coating appears to be composed of near-spherical nanocrystals of 5–10 nm, which correlates with the average crystallite size found through the XRD analysis.

The LSMO thickness was confirmed by the elemental composition EDS profile scanned across the LSMO/BCNT, where the BCNT core and LSMO shell are clearly distinguished (see Fig. 3c). The HR-TEM lattice fringes correspond to LSMO planes, such as the {112} and {220} planes with *d*-spacings of 2.737 and 1.901 Å, respectively. This is also supported by the SAED rings, which are indexed to the orthorhombic perovskite structure of polycrystalline LSMO in agreement with the X-ray diffractograms and Raman spectra (see Fig. 3d–e). These results are consistent with the conformal coating of LSMO on the outer surface of BCNTs as further revealed in the EF-TEM elemental mapping of LSMO (see Fig. 3f). This mapping allows us to distinguish the presence of LSMO crystallites all around the BCNTs, comprising a conformal coating. At the interface of LSMO/BCNT, it is reasonable to propose that the oxygen-terminated MnO_6 edges of nano-sized LSMO crystals are linked to carbon atoms, which preferentially forms a stable metal carbonyl, during the vaporization of the LSMO target (plasma plume). Such "back-

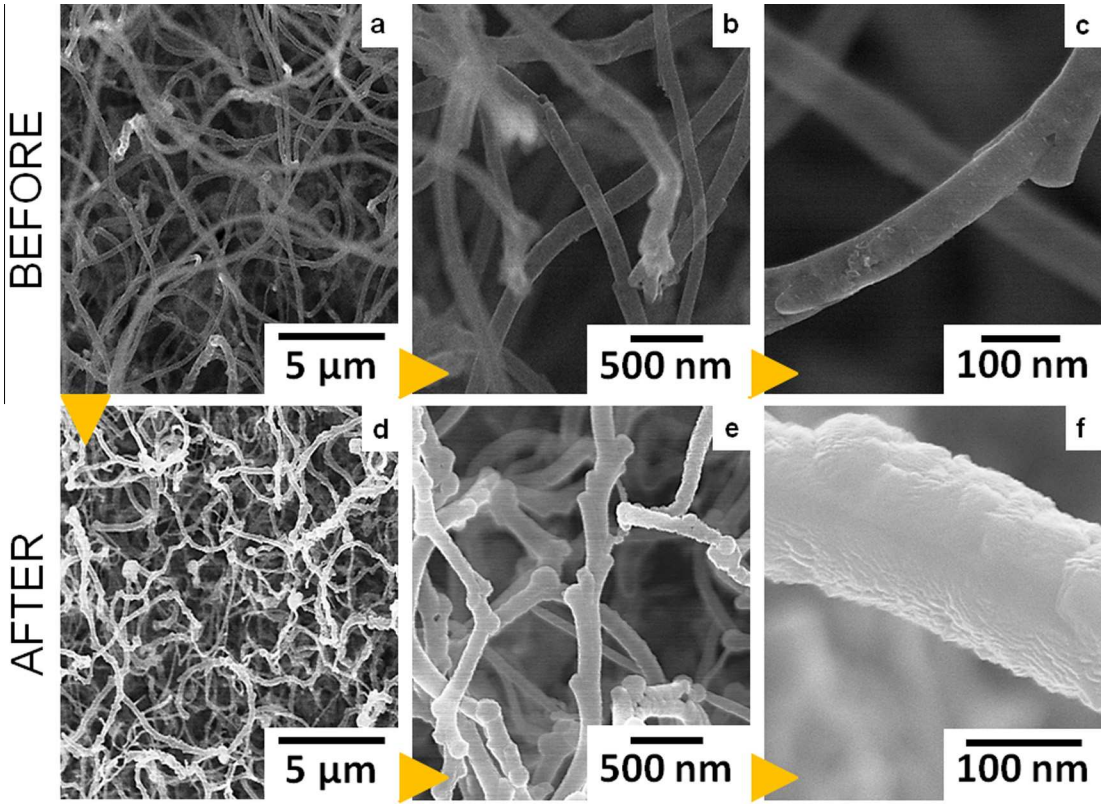

Fig. 2 – FE-SEM images of BCNTs before (a–c) and after (d–f) the pulsed-laser deposition of LSMO. Isolated BCNT and LSMO/BCNT show uniformity and conformal coating, respectively. A colour version of this figure can be viewed online.

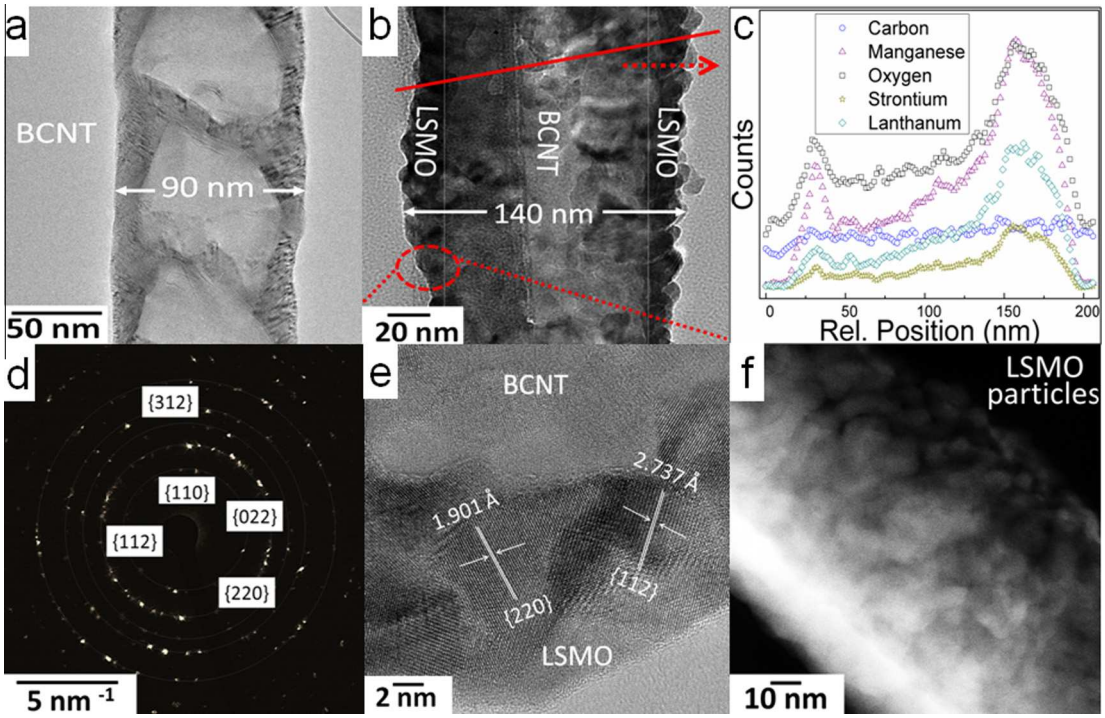

Fig. 3 – TEM image (a) of individual BCNT before deposition. HR-TEM images (b, e), line-scanned EDS profile (c), SAED rings (d) and EF-TEM map (f) of individual LSMO/BCNT.

bonding" is known to form in a reducing atmosphere at relatively low pressure [27], similar to the conditions employed here in the synthesis process.

We have conducted RT electrical transport measurements on both individual LSMO/BCNT and BCNT via *in situ* electrical probing in order to explore the effect of LSMO on the electrical response of BCNT. The setup employed (see Fig. 4a), was placed inside the TEM chamber. Fig. 4b shows the TEM image of an individual LSMO/BCNT structure mounted on this setup, connected to a stationary Au metal wire and subsequently to a movable Au STM tip. An almost symmetric *I*–*V* curve was obtained for both LSMO/BCNT and BCNT (see Fig. 4c–d), probably due to the effective contact area and the proper barrier heights [28]. A more-pronounced zero-current gap in the low bias regime was observed for BCNT which is attributed to its semiconducting nature. Both curves exhibit a power-law character (solid lines), $I \sim (V_{bias})^n$, with n between 1 and 9; such values of n correspond to semiconducting CNTs [3]. It was also found that the current in LSMO/BCNT increased by one order of magnitude when compared to BCNT.

Although such semiconducting features of LSMO/BCNT depend strongly on the contacts and nanotube geometry, these contact effects can be effectively decoupled from the experimental data. Further intrinsic electrical parameters of LSMO/BCNT can be extracted. To do this, the metal-semiconductor-metal (MSM) model is elicited [28–31]. The validity of this model lies in the fact that the transport can be considered to be mainly diffusive and that the use of depletion approach as a first approximation is applicable. To ensure the diffusive regime, LSMO/BCNT and BCNT of ~1 μm in length were employed. In practice, this model relies on the similarities of both the forward and reversed-biased slopes of the corresponding *I*–*V* curves. The actual difference in forward and reversed-biased slopes is <1% for LSMO/BCNT and <3% for BCNT, which validates the use of this model. Moreover, the transport in semiconducting CNTs is remarkably described by MSM (independent of the gate voltage), which involves two contacts connected in series to a resistor (nanotube) in between and dominated by the reverse-biased Schottky barrier at low bias and by the semiconducting CNT at large bias [28–31]. We assume throughout the calculations that the contacts formed at the nanotube terminals are Schottky-like. Accordingly, the resistances can be determined assuming that the current at high bias regime (700–1000 mV) is totally distributed across the LSMO/BCNT approaching to a straight line with a slope given by the resistance, $R \approx dV/dI$. The resistances of LSMO/BCNT and BCNT obtained through this procedure yield 0.28 and 1.09 MΩ, respectively, as shown in the lower insets of Fig. 4c–d. The resistivities were determined to be 0.43 and 0.69 Ω·cm for LSMO/BCNT (~1 μm in length and 140 nm in diameter) and BCNT (~1 μm in length and 90 nm in diameter), respectively. The value of resistivity for LSMO/BCNT is comparable to that reported for thin films of LSMO [32] and an order of magnitude lower than that of LSMO particles of 40–80 nm [33]. This result indicates that the transport in the LSMO coating is not dominated by intergranular resistivity, which could be ascribed to thinner inter-grain separation produced by PLD that in turn facilitates electron hopping. The resistivity in BCNT is two orders of magnitude greater than that of typical MWCNTs [34] due to the fact that BCNTs are not structurally perfect (e.g., significant curvature and pentagonal or heptagonal defects), the annular cross-section area is not considered for calculations, the individual shells behave as metallic, semiconducting or insulating

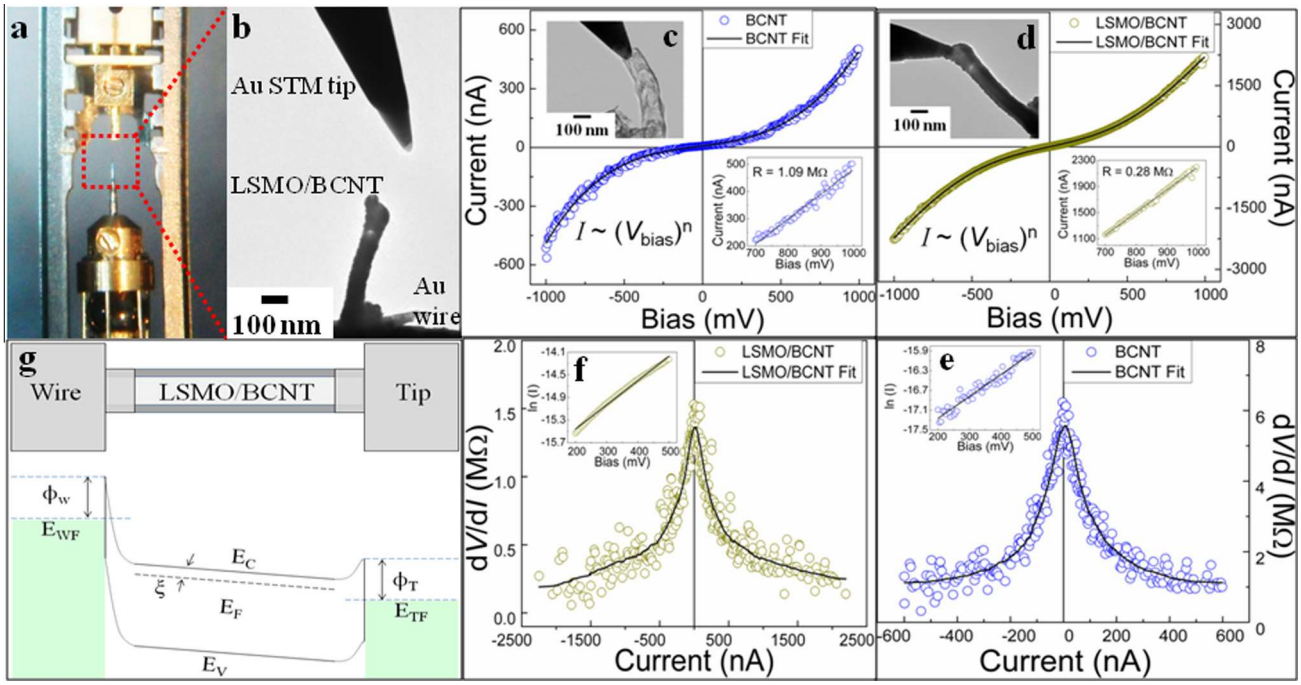

Fig. 4 – Optical image of the STM-TEM holder setup, (a) STM-TEM setup as viewed under the TEM (b) aggregated *I–V* curves for BCNT (c) and LSMO/BCNT (d) along with their corresponding TEM images and their aggregated *I–V* curves at high bias regime (insets, fits in solid lines). Concurrent d*V*/d*I* curves for BCNT (e) and LSMO/BCNT (f) along with their corresponding ln *I* vs *V* plots in the intermediate bias regime (inset, fits in solid lines). Schematic and band diagrams of the MSM (g) showing the bending of bands at the interfaces under bias.

indistinctly, and the defects increase the resistivity through electron scattering [34]. In fact, BCNTs structural characteristics are distinct to those of MWCNTs and their shells manifest different helicity. As shown in our HRTEM analysis, BCNTs present a high density of defects (i.e., bamboo defects), which arise both from the interruption and separation of inner shells by fullerenic semi-spheres and from the continuity of outer shells [35]. These structural features therefore cause a substantial increase in the resistivity and a decrease in the axial conduction of BCNT. Nonetheless, according to the experimental data, an enhancement of the electrical current was achieved by depositing conformally-coated LSMO on the outer layer of BCNTs. This may be due to that a significant amount of defects of BCNTs are depleted by the LSMO coating and that extra hot carriers are injected into the circuit from LSMO to BCNTs. The current across LSMO/BCNT turned out to be two orders of magnitude greater than the 120 nm-thick LSMO nanowires under ±1000 mV and one order of magnitude greater than nano-sized LSMO subject to ±600 mV [14,36]. The LSMO/BCNT and BCNT resistances were further confirmed and extended over all the bias regimes via the numerical differentiation of *I-V* curves where $R = dV_{nt}/dI \approx dV/dI$, yielding 0.2–1.4 and 0.9–5.2 MΩ, respectively, with V_{nt} being the voltage drop across the channel (see Fig. 4e–f). These values are consistent with those obtained by the MSM modeling at high bias regime.

Additional intrinsic electrical parameters of LSMO/BCNT and BCNT can be obtained at intermediate bias (200–500 mV), where the total current *I* is dominated by the reverse-biased Schottky barrier. Such tunneling current is essentially the thermionic-field emission current [28,30] and can be calculated (neglecting any leakage current) via

$$\ln I = \ln I(SJ) = \ln S + V\left(\frac{q}{kT} - \frac{1}{E_0}\right) + \ln J_s \quad (1)$$

with S, *J*, E_o and J_s being the Schottky-barrier contact area, the current density through the Schottky barrier, a parameter and a slowly varying function of the model, respectively. The parameter E_o can be obtained empirically by means of the slope q/kT-$1/E_o$ from the logarithmic plot of *I–V* curve, as observed in the insets of Fig. 4e–f, which follow a linear relationship. Likewise, E_o is given by

$$E_o = E_{oo}\coth\left(\frac{qE_{oo}}{kT}\right) \quad (2)$$

where E_{oo} in tunneling theory physically represents the diffusion potential of the Schottky barrier such that the transmission probability for an electron whose energy coincides with the bottom of the conduction band at the edge of the depletion region is equal to 1/e [30]. E_{oo} can be expressed by the following equation:

$$E_{oo} = \frac{\hbar}{2}\left(\frac{N_d}{m_n^*\varepsilon_s\varepsilon_o}\right)^{1/2} \quad (3)$$

with N_d, m_n^*, ε_s and ε_o being the effective doping concentration at the metal/semiconductor interface, the effective mass of the electron, the relative permittivity of the semiconductor, and the permittivity of free space, respectively. The electron density *n* (assumed to be the same as N_d) can be derived considering that E_{oo} is presumably in the order of kT/*q*, since the transport mechanism is thermionic-field emission. Thus, *n* at

Table 1 – Main parameters obtained through the MSM model for individual LSMO/BCNT and BCNT. m_n^*, m_h^* and ε_s were assumed to be the same as their bulk counterparts [37–40].

Sample	Diameter [nm]	Current [nA]	Resistivity [Ω cm]	Electron density [cm^{-3}]	E_g [eV]
BCNT	90	600	0.69	1.27×10^{18}	0.31
LSMO/BCNT	140	2500	0.43	1.40×10^{22}	0.15

RT is obtained in turn from E_{oo} and E_o resulting in $n = 1.40 \times 10^{22}$ and $n = 1.27 \times 10^{18}\ cm^{-3}$ for LSMO/BCNT and BCNT, respectively, which are consistent with those of ordinary LSMO and graphitic structures [29,37]. Additionally, the band gap is extracted from

$$n_i = \left[\frac{(kT)^{3/2}(m_n^* m_h^*)^{3/4}}{2(2\pi\hbar^2)^{3/2}}\right]\exp\left(-\frac{E_g}{2kT}\right) \quad (4)$$

where n_i, m_h^* and E_g are the concentration of carriers in an intrinsic semiconductor, the effective mass of holes, and the band gap, respectively [30]. By introducing the values of n_i in this expression, one obtains $E_g = 0.15$ and $E_g = 0.31$ eV for LSMO/BCNT and BCNT, respectively, which are compatible with those of perovskite oxides and semiconducting CNT [37,39]. The band gap calculated for BCNT contrasts with that of gapless epitaxial graphene. This difference is ascribed to the high density of bamboo-like defects presented in BCNT and the fact that a large portion of the reactive edges of BCNT are exposed. It is probable that such defects alter the density of states and supply with an excess of charge to the edges making BCNT more semiconducting [29]. Note that the bulk values of m_n^*, m_h^* and ε_s [32,39–41] were employed for these calculations and that both n and E_g of LSMO/BCNT depend exclusively upon such physical constants. Our calculations (see Table 1 for LSMO) suggest that the conduction parameters of LSMO/BCNT do not change significantly, considering both of their constituents, and that the electronic transport is not only along or across the inner layers, but also mainly along the outer layer of LSMO. This may be explained by the fact that charge carriers undergo less scattering through LSMO and their effective masses depend on lattice direction [42]. To justify that the contacts in LSMO/BCNT are Schottky-like but not identical to conventional Schottky contacts, a simple rationale is proposed. At an interface, the standard semiconductor theory foresees an electronic band bending when the density of interface states is high regardless of the electrode work function and the pinning of the Fermi level [43]. The barrier width and height of such band bending hinge upon the net charge of the interface states and their energetic distribution in the band gap. It is reasonable to think that the contact resistance due to the nano-sized STM probing, the bundle resistance at the base (which is high due to scattering and resistive heating), and the intermediate electronegativity of BCNT might favor the removal of a considerable amount of oxygen from the contact surface of LSMO. This would in turn generate a high density of intermediate states and, consequently, band bending at the interface of both contacts. One would thus expect that upon applying an intermediate voltage across the interfaces, the majority of electrons would be distributed into the interface states under reverse bias, while the minority would do the same under forward bias, just as predicted by the MSM model. Thereby, a Schottky-like barrier is formed in both contacts in contrast to the metal-to-metal contact. A qualitative band diagram is shown in Fig. 4g, wherein the band bending at the wire-LSMO/BCNT and LSMO/BCNT-tip interfaces under bias is displayed. ϕ_w, ϕ_T, E_{WF} E_{TF}, E_C, E_F, E_V and ξ denote the Schottky barrier heights associated to the wire-LSMO/BCNT and LSMO/BCNT-tip contacts, the Fermi levels of the wire and tip electrodes, the conduction and valence bands, the Fermi level of the semiconducting LSMO/BCNT, and the distance between the bottom of E_C and E_F, respectively. Similar findings via this oxygen-defect-produced-interface-state-induced band bending picture were drawn for metal/perovskite manganite interfaces and metal/ferrolectric oxide interfaces [44–47]. Nonetheless, the origin of such formation remains unclear and further study is needed to elucidate the mechanism.

4. Conclusion

We have developed a straightforward synthesis process to produce high-quality ferromagnetic-on-carbon nanotube LSMO/BCNT hybrid structures without causing any deterioration to the BCNT. The synthesis protocol described here can be extended to integrate other oxides not only on CNTs but also on numerous types of supporting materials. The individual *I–V* characteristics of LSMO/BCNT were probed via *in situ* STM-TEM. Modeling of the *I–V* data assuming the MSM configuration was used to obtain the resistivity, band gap and electron density of the LSMO and BCNT. The transport properties of individual LSMO/BCNT were found to outperform those of BCNT alone. This breakthrough enables the integration of oxide materials onto CNTs as an important step towards nanoelectronics. It can lead to the fabrication of one-dimensional core-multishell materials with intriguing multifunctional features, such as colossal magnetoresistance, multiferroic, superconducting and nonlinear-optical properties. By enabling the integration of spintronic materials and carbon nanotubes, this study advances the utilization of an extra degree of freedom, spin, into conventional charge-based electronic devices, which will be critical in generating integration densities higher than those of conventional semiconductor devices, decreasing the electric power consumption and increasing the data processing speed. This prospect and the elucidation of spin-polarized currents, the detection of spin polarization, and the efficiency of electrical spin injection will be explored in a future work.

Acknowledgments

This work was supported in part by the Institute for Functional Nanomaterials (NSF Grant # 1002410), PR NASA EPSCoR

(NASA Cooperative Agreement #NNX13AB22A) and PR DOE EPSCoR (DOE Grant # DEFG02-08ER46526). We gratefully acknowledge the high-resolution electron microscopy images provided by Dr. Maxime J.-F. Guinel. J.C.-N. thanks the NASA Office of the Chief Technologist's Space Technology Research Fellowship Grant No. NNX11AN21H.

REFERENCES

[1] Aviram A, Ratner MA. Molecular rectifiers. Chem. Phys. Lett. 1974;29:277–83.
[2] Kong J, Yenilmez E, Tombler TW, Kim W, Dai H, Laughlin RB, et al. Quantum interference and ballistic transmission in nanotube electron waveguides. Phys. Rev. Lett. 2001;87:106801.
[3] Tans SJ, Verschueren ARM, Dekker C. Room-temperature transistor based on a single carbon nanotube. Nature 1998;393:49–52.
[4] Dresselhaus MS. Nanotubes: a step in synthesis. Nat. Mater. 2004;3:665–6.
[5] Zhu J, Jia J, Kwong F, Leung DH. Synthesis of bamboo-like carbon nanotubes on a copper foil by catalytic chemical vapor deposition from ethanol. Carbon 2012;50:2504–12.
[6] Endo M, Kim YA, Ezaka M, Osada K, Yanagisawa T, Hayashi T, et al. Selective and efficient impregnation of metal nanoparticles on cup-stacked-type carbón nanofibers. Nano Lett. 2003;3:723–6.
[7] Heng LY, Chou A, Yu J, Chen Y, Gooding JJ. Demonstration of the advantages of using bamboo-like nanotubes for electrochemical biosensor applications compared with single walled carbon nanotubes. Electrochem. Commun. 2005;7:1457–62.
[8] Lee CJ, Park JH, Park J. Synthesis of bamboo-shaped multiwalled carbon nanotubes using thermal chemical vapor deposition. Chem. Phys. Lett. 2000;323:560–5.
[9] Saito Y. Nanoparticles and filled nanocapsules. Carbon 1995;33:979–88.
[10] Hueso LE, Pruneda JM, Ferrari V, Burnell G, Valdes-Herrera JP, Simons BD, et al. Transformation of spin information into large electrical signals using carbón nanotubes. Nature 2007;445:410–3.
[11] Hueso LE, Burnell G, Prieto JL, Granja L, Bell C, Kang DJ, et al. Electrical transport between epitaxial manganites and carbon nanotubes. Appl. Phys. Lett. 2006;88:083120.
[12] Mieville L, Worledge D, Geballe TH, Contreras R, Char K. Transport across conducting ferromagnetic oxide/metal interfaces. Appl. Phys. Lett. 1998;73:1736–40.
[13] Levy P, Leyva AG, Troiani HE, Sanchez RD. Nanotubes of rare-earth manganese oxide. Appl. Phys. Lett. 2003;83:5247–9.
[14] Jugdersuren B, Kang S, DiPietro RS, Heiman D, McKeown D, Pegg IL, et al. Large low field magnetoresistance in $La_{0.67}Sr_{0.33}MnO_3$ nanowire devices. Appl. Phys. 2011;109:016109.
[15] Carretero-Genevrier A, Mestres N, Puig T, Hassini A, Oró J, Pomar A, et al. Single-crystalline $La_{0.7}Sr_{0.3}MnO_3$ nanowires by polymer-template-directed chemical solution synthesis. Adv. Mater. 2008;20:3672–7.
[16] Miyazaki K, Kawakita K, Abe T, Fukutsuka T, Kojima K, Ogumi Z. Single-step synthesis of nano-sized perovskite-type oxide/carbon nanotube composites and their electrocatalytic oxygen-reduction activities. J. Mater. Chem. 2011;21:1913–7.
[17] Lee KW, Lee CE, Gedanken A, Sominski E, Koltypin Y. Triggering a metal-insulator transition in $La_{0.8}Sr_{0.2}MnO_3$ nanoparticle-decorated carbon nanotubes. J. Korean Phys. Soc. 2011;59(6):3309–13.
[18] Morell G, Canales E, Weiner BR. In situ measurements of methane and acetylene concentrations in a CVD reactor by infrared spectroscopy. Diam. Rel. Mater. 1999;8:166–70.
[19] Beltran-Huarac J, Martinez R, Palai R. Magnetoelectric properties of BST/LSMO particulate composites. 2011 MRS Spring Meeting and Exhibit. San Franscisco (California. USA): Materials Research Society, 2011; 1368, p. 3.
[20] Boyle MG, Feng L, Dawson P. Safe fabrication of sharp gold tips for light emission in scanning tunneling microscopy. Ultramicroscopy 2008;108:558–66.
[21] Iliev MN, Abrashev MV, Lee HG, Popov VN, Sun YY, Thomsen C, et al. Raman spectroscopy of orthorhombic perovskite $YMnO_3$ and $LaMnO_3$. Phys. Rev. B 1998;57:2872–7.
[22] Tuinstra F, Koenig JL. Raman spectrum of graphite. J. Chem. Phys. 1970;53:1126–30.
[23] Mendoza F, Kumar A, Martinez R, Scott JF, Weiner B, Katiyar RS, et al. Conformal coating of ferroelectric oxides on carbon nanotubes. EPL 2012;97:27001.
[24] Kumar A, Shivareddy SG, Correa M, Resto O, Choi Y, Code MT, et al. Ferroelectric-carbon nanotube memory devices. Nanotechnology 2012;23:165702.
[25] Han S, Li C, Liu Z, Lei B, Zhang D, Jin W, et al. Transition metal oxide core-shell nanowires: Generic synthesis and transport studies. Nano Lett. 2004;4:1241–6.
[26] Li C, Lei B, Luo Z, Han S, Liu Z, Zhang D, et al. Magnetoresistive $La_{0.67}Sr_{0.33}MnO_3$ nanowires. Adv. Mater. 2005;17:1548–53.
[27] Cesarea M, Caricato AP, Maruccio G, Martino M. LSMO - growing opportunities by PLD and applications in spintronics. J. Phys. Conf. Ser. 2011;292:012003.
[28] Zhang ZY, Jin CH, Liang XL, Chen Q, Peng LM. Current–voltage characteristics and parameter retrieval of semiconducting nanowires. Appl. Phys. Lett. 2006;88:073102.
[29] Liu Q, Ren W, Chen ZG, Yin L, Li F, Cong H, et al. Semiconducting properties of cup-stacked carbon nanotubes. Carbon 2009;47:731–6.
[30] Zhang ZY, Yao K, Liu Y, Jin CH, Liang XL, Chen Q, et al. Quantitative analysis of current–voltage characteristics of semiconducting nanowires: Decoupling of contact effects. Adv. Funct. Mater. 2007;17:2478–89.
[31] Padovani FA, Stratton R. Field and thermionic-field emission in Schottky barriers. Solid-State Electron. 1966;9:695–707.
[32] Salamon MB, Jaime M. The physics of manganites: Structure and Transport. Rev. Mod. Phys. 2001;73:583–628.
[33] Cuong PV, Kim DY. Effect of strontium doping level on electrical transport and magnetic properties of $La_{1-x}Sr_xMnO_3$ perovskite nanoparticles. J. Phys. Conf. Ser. 2009;187:012090.
[34] Dai H, Wong EW, Lieber CM. Probing electrical transport in nanomaterials: Conductivity of individual carbon nanotubes. Science 1996;272:523–6.
[35] Iijima S, Ajayan PM, Ichihashi T. Growth model for carbon nanotubes. Phys. Rev. Lett. 1992;69:3100–3.
[36] Murakami Y, Kawamoto N, Shindo D, Ishikawa I, Deguchi S, Yamazaki K, et al. Simultaneous measurements of conductivity and magnetism by using microprobes and electron holography. Appl. Phys. Lett. 2006;88:223103.
[37] Tiwari A, Jin C, Kumar D, Narayan J. Rectifying electrical characteristics of $La_{0.7}Sr_{0.3}MnO_3$/ZnO heterostructure. Appl. Phys. Lett. 2003;83:1773–5.
[38] Zhao K, Jin K, Lu H, Huang Y, Zhou Q, He M, et al. Transient lateral photovoltaic effect in p-n heterojunctions of $La_{0.7}Sr_{0.3}MnO_3$ and Si. Appl. Phys. Lett. 2006;88:141914.
[39] Qiu J, Jin K, Han P, Lu H, Hu C, Wang B, et al. A theoretical study on the transport property of the $La_{0.7}Sr_{0.3}MnO_3$/Si p-n heterojunction. EPL 2007;79:57004.
[40] Marulanda JM, Srivastava A. Carrier density and effective mass calculations in carbon nanotubes. Phys. Stat. Sol. B 2008;245:2558–62.

[41] Lu W, Wang D, Chen L. Near-static dielectric polarization of individual carbon nanotubes. Nano Lett. 2007;7:2729–33.
[42] Lu YH, Muñoz M, Steplecaru CS, Hao C, Bai M, Garcia N, et al. Electrostatic force microscopy on oriented graphite surfaces: Coexistence of insulating and conducting behaviors. Phys. Rev. Lett. 2006;97:076805.
[43] Sze SM, Kwok KN. Physics of Semiconductor Devices. Third ed. New Jersey: John Wiley & Sons; 2007. 134–96.
[44] Sawa A, Fuji T, Kawasaki M, Tokura Y. Interface resistance switching at a few nanometer thick perovskite manganite active layers. Appl. Phys. Lett. 2006;88:232112.
[45] Blom PWM, Wolf RM, Cillessen JFM, Krijin MPCM. Ferroelectric Schottky diode. Phys. Rev. Lett. 1994;73:2107.
[46] Schmehl A, Lichtenberg F, Bielefeldt H, Mannhart J, Schlom DG. Transport properties of $LaTiO_{3+x}$ films and heterostructures. Appl. Phys. Lett. 2003;82:3077.
[47] Sawa A, Fuji T, Kawasaki M, Tokura Y. Hysteretic current–voltage characteristics and resistance switching at a rectifying $Ti/Pr_{0.7}Ca_{0.3}MnO_3$ interface. Appl. Phys. Lett. 2004;85:4073–5.